

Received 27 October 2023, accepted 14 November 2023, date of publication 21 November 2023, date of current version 29 November 2023.

Digital Object Identifier 10.1109/ACCESS.2023.3335372

RESEARCH ARTICLE

LPMsDE: Multi-Scale Denoising and Enhancement Method Based on Laplacian Pyramid Framework for Forward-Looking Sonar Image

ZHISEN WANG^{1,2}, ZHUOYI LI³, XUANXUAN TENG⁴, AND DESHAN CHEN^{1,2,5}

¹State Key Laboratory of Maritime Technology and Safety, Wuhan University of Technology, Wuhan 430063, China

²National Engineering Research Center for Water Transport Safety, Wuhan University of Technology, Wuhan 430063, China

³Department of Logistics and Maritime Studies, The Hong Kong Polytechnic University, Hong Kong, China

⁴School of Electric and Electronic Engineering, Wuhan Polytechnic University, Wuhan 430023, China

⁵Intelligent Transportation Systems Research Center, Wuhan University of Technology, Wuhan 430063, China

Corresponding authors: Xuanxuan Teng (tengxuanxuan@whpu.edu.cn) and Deshan Chen (dschen@whut.edu.cn)

This work was supported in part by the National Key Research and Development Program of China under Grant 2023YFC3010803, in part by the National Natural Science Foundation of China under Grant 52272424, in part by the Key Research and Development Program of Hubei Province of China under Grant 2023BCB123, in part by the Science Foundation of Educational Commission of Hubei Province of China under Grant Q20191607, and in part by the Fundamental Research Funds for the Central Universities under Grant WUT:2023IVB079.


ABSTRACT Forward-looking sonar (FLS) images present various challenges in interpretation, recognition, and segmentation due to limitations like low resolution, speckle noise, and low contrast, making them more complex than optical images. Existing methods often focus solely on denoising or enhancement, neglecting the potential benefits of utilizing multi-scale features to create an integrated image processing approach. This paper introduces the Laplacian pyramid-based multi-scale denoising and enhancement (LPMsDE) method tailored for FLS images. The proposed method begins by presenting a novel multiplicative speckle noise model, grounded in the Gaussian distribution, specifically designed for FLS images. Next, the Laplacian pyramid decomposition is utilized to estimate noise variance, with an modified adaptive local filter. Lastly, a combination of the Laplacian pyramid framework, the enhanced adaptive local filter, and Contrast-Limited Histogram Equalization (CLHE) is employed to denoise and enhance images at different resolution levels. Through comprehensive experiments conducted on both simulated and real sonar images, the effectiveness of the LPMsDE method is demonstrated. It surpasses other denoising and enhancement techniques, as evidenced by superior scores in Structural Similarity Index (SSIM), Peak Signal-to-Noise Ratio (PSNR), Contrast-to-Noise Ratio (CNR), Equivalent Number of Looks (ENL), Natural Image Quality Evaluator (NIQE), and Blind/Referenceless Image Spatial Quality Evaluator (BRISQUE).

INDEX TERMS Forward-looking sonar, speckle noise, image denoising, contrast enhancement, multi-scale analysis, Laplacian pyramid.

I. INTRODUCTION

The absorption coefficient of acoustic waves in water is significantly smaller than that of light waves and electromagnetic waves. As a result, sonar devices find widespread applications in underwater activities, as they are unaffected by the turbidity and optical visibility of water. Among the

popular underwater detection devices, forward-looking sonar (FLS) stands out. The FLS system employs sonar sensors that emit acoustic waves, which, upon reflection from objects in the water, generate visual images of the underwater environment, akin to optical camera images [1]. Typically mounted at the front of ships or vehicles, FLS systems offer valuable situational awareness, obstacle avoidance, and navigation information. They serve diverse purposes, including marine navigation, underwater search and rescue operations,

The associate editor coordinating the review of this manuscript and approving it for publication was Chengpeng Hao .

underwater exploration, military applications like mine detection, and the tracking of submarines [2].

The underwater environment presents unique complexities, affecting the echo signals received by sonar. Factors such as channel propagation loss, environmental noise, and multipath effects lead to low resolution, blurred target edges, and significant noise in sonar images [3]. Over the past decades, advancements in sensor sensitivity and digital beamforming and image processing technologies have considerably improved the overall quality of FLS images. Nevertheless, various noise types persist, making it challenging to interpret the images and impacting the efficacy of scene analysis algorithms, such as image segmentation, underwater object detection, and recognition [4]. Consequently, reducing noise in FLS images and enhancing their quality serve as the foundation for further advancements in FLS imaging.

Existing denoising methods for sonar images can be classified into two categories: traditional methods and deep learning methods. Traditional methods can be further divided into two categories based on the different denoising principles: spatial domain methods and transform domain/sparse representation methods.

In the early stages of image processing techniques, spatial operations employed simple structural filters like the Lee filter [5], Frost filter [6], and Kuan filter [7]. However, these methods tend to lose edge information during the denoising process. Subsequently, approaches considering other factors emerged, such as bilateral filtering based on grayscale differences between pixels [8] and anisotropic diffusion filtering based on gradient information [9]. Currently, the forefront of research in spatial domain methods involves denoising algorithms based on local self-similarity, leveraging inherent redundancy and regularity in natural images. The mainstream denoising algorithms include non-local means filtering (NLM) [10], block-matching and 3D filtering (BM3D) [11], along with their improved versions. For instance, Abu and Diamant proposed an adaptive NLM filter that models noise in different regions using distinct distributions [12]. Han et al. introduced an improved BM3D algorithm that adapts its parameters based on the noise characteristics of sonar images. Additionally, they incorporated a Gaussian filter and gray correction before the basic estimation [13]. As the performance improves, the complexity of these denoising algorithms has also increased, resulting in an increase in the number of parameters which need to be manually set. Inappropriate parameters will seriously affect the denoising performance, limiting the robustness of these algorithms.

Transform domain methods and sparse representation methods fall into the same category, as they both involve representing the image as a linear combination of a set of basis functions, effectively separating useful information from noise initially mixed uniformly together [14]. Various researchers have explored wavelet domain denoisers for sonar images, employing different thresholding methods

[15]. Others utilized the dual-tree complex wavelet transform (DT-CWT) and three variants of the BiShrink filter to reduce speckle noise [16]. Additionally, researchers proposed enhancement algorithms in the wavelet domain, employing techniques like Gaussian mixture model and Gaussian mixture model to preserve weak feature information in sonar images [17]. Further, adaptive soft threshold denoisers were designed for sonar water column images, employing mathematical features of all angle sequences to divide the water column data into background areas and target-noise mixing areas [18]. Denoising methods based on principal component analysis (PCA) and singular value decomposition (SVD) have also been proposed [19], showing usefulness in preprocessing sonar images for underwater target tracking algorithms [20]. Other transform domain methods, including curve transform [21], [22], discrete cosine transform (DCT) [23], Radon transform [24], and shearlet transform [25], have been applied to sonar image denoising as well. Existing transform domain methods have not effectively utilized the multi-scale characteristics of the FLS image. The images in the transformed domain are difficult to visually comprehend, posing challenges for analyzing the characteristics of different scales. Currently, there is a lack of a transform method that can effectively achieve image multi-scale analysis.

Among denoising methods based on image sparse representation, researchers developed a novel sub-bottom profile image denoising method, utilizing a non-local low-rank framework to obtain underlying clean images [26]. A model combining nonconvex total variation regularization and generalized Kullback-Leibler fidelity was presented for sonar image denoising [27]. Similarly, a generalized low-rank model for Cauchy noise removal was introduced, and a proximal alternating algorithm was developed to solve the nonconvex model [28]. However, sparse representation-based methods also have some limitations, such as sensitivity to noise, dependence on accurate and suitable dictionaries, and high computational complexity.

In recent years, deep learning has made remarkable strides in various image-related tasks, such as image restoration [29], semantic segmentation [30], object detection [31]. Supervised learning methods optimize network weights by minimizing the distance between noisy inputs and clean targets. For instance, Kim et al. developed a neural network with auto-encoder structures to enhance sonar images, verified using acoustic lens-based multibeam sonar images [32]. Sung et al. employed a convolutional neural network to detect and remove crosstalk noise in forward scan sonar images [33]. Additionally, a denoising and segmentation network integrating the Receptive Field Block and Attention Search Function was proposed [34]. Lee et al. presented a deep learning-based compressive sensing method with enhanced nonlinearity using an iterative shrinkage and thresholding algorithm for denoising side-scan sonar images [35]. However, noise-free sonar images are rare, leading supervised training methods to use clean optical images as ground

truth and artificially noised versions as input noise images. This creates a domain gap between synthetic data and real sonar images, leading to artifacts or loss of potential information [36]. Self-supervised learning methods have shown promise as an effective denoising solution [37]. These methods employ a blind convolutional network structure to efficiently process noisy versions of each image in the dataset and reconstruct clean pixels from adjacent pixels [38], [39]. Nonetheless, due to the lack of clean FLS images, self-supervised learning does not guarantee training results approaching the clean image. The majority of deep learning algorithms rely on high-quality training data and may suffer from overfitting, while traditional methods tend to be more robust and generalizable.

In this paper, we propose a novel Laplacian pyramid-based multi-scale denoising and enhancement (LPMsDE) method. Leveraging the Laplacian pyramid framework, the image is decomposed into multiple high-frequency components and one low-frequency component. Based on the distinct characteristics of each component, appropriate denoising and enhancement methods are selected, and the image is reconstructed using the Laplacian pyramid inverse transform. During the denoising process, a modified adaptive local filter and a novel FLS multiplicative speckle noise model are employed.

The contributions of this work encompass three main aspects:

- 1) A reliable yet simple Gaussian distributed FLS image multiplicative speckle noise model is proposed and its effectiveness demonstrated through pixel value frequency statistics.
- 2) By exploring the relationship between Laplacian image variance and real image noise variance, a modified adaptive local filter is proposed, utilizing Laplacian images to estimate noise variance.
- 3) A multi-scale denoising and enhancement method based on the Laplace pyramid framework is proposed. Modified adaptive local filtering and contrast limited histogram equalization are used to denoise and enhance the high-frequency and low-frequency components, respectively.

The paper is organized into five main sections. Section I introduces the FLS image denoising and enhancement, presenting an overview of related work. Section II delves into the multiplicative noise model in FLS images. Section III describes the proposed LPMsDE method. Section IV presents experimental results and analysis. Finally, Section V concludes the paper's findings.

II. FLS SPECKLE NOISE MODEL

In this section, we try to present and analyze a reliable FLS speckle noise model and analyze the statistical properties of noise in FLS images. Such analysis provides a deeper understanding of noise characteristics and distribution and enables the development of more targeted denoising methods.

Moreover, a reliable noise model allows for the creation of simulated sonar images by introducing noise to artificial images, thus augmenting the currently limited dataset.

In spite that several speckle noise models have been proposed [25], [40], [41], a speckle noise model conforming to the unique characteristics of FLS has been lacking. In this paper, we propose an FLS speckle noise model that enables the generation of artificial noise, aligning with the real FLS noise characteristics, and facilitates noise variance estimation through adaptive local filtering in subsequent sections.

To maintain the model's generalization and simplicity, we do not explicitly model the actual processes of acoustic signal generation and propagation affected by noise. Instead, we analyze the abstract sources of noise in FLS images. Inspired by [40], the noise in FLS images can be represented as Equation (1):

$$\varphi(x, y) = \omega_m(x, y)\psi(x, y) + \omega_a(x, y) \quad (1)$$

where $\varphi(x, y)$ denotes the observed noisy image obtained in practical scenarios, while $\psi(x, y)$ represents the potential pure image unaffected by noise under ideal conditions. Additionally, $\omega_m(x, y)$ and $\omega_a(x, y)$ respectively denote the multiplicative and additive noise components.

The intensity of multiplicative portion in Equation (1) is positively correlated with the echo intensity of sonar signals, making it the primary component in general [41]. Speckle noise is widely observed in synthetic aperture radar, medical ultrasound, and sonar images [42], [43], and it essentially represents an interference phenomenon of waves. When the acoustic waves emitted by the imaging sonar encounter rough structures on the surface of an object, a large number of scattered sub-waves are generated, overlapping with each other in space. If two sub-waves reach the sonar receiving array at their peak positions, their vibrations combine to form a bright spot in the sonar image. Conversely, if one sub-wave is at its peak position, and the other is at its trough position, they cancel each other out, resulting in no acoustic waves being received in that direction, forming a dark spot in the image. Due to the large number of scattered sub-waves and their highly random phase distribution, these echoes create numerous randomly distributed bright and dark spots in the image, known as speckle noise.

In comparison to the multiplicative component, the sources of additive noise are more complex, encompassing random noise distributed underwater (such as marine biological sounds and sonar carrier motion noise), underwater impurities and small bubbles, structural noise generated during FLS operation, and Gaussian white noise in the channel during signal transmission, among others [44].

The intensity of the acoustic signal $\psi(x, y)$ used utilized for FLS perception far exceeds that of additive noise, while the intensity of the multiplicative noise is directly proportional to the acoustic signal intensity. Consequently, the impact of additive noise on the image is minimal compared to that of multiplicative noise. To simplify the noise model and reduce its complexity, the additive noise is excluded. Thus,

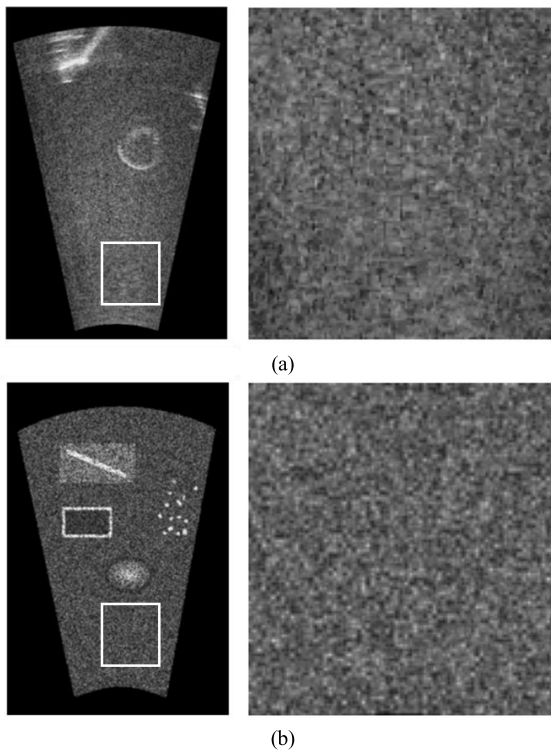


FIGURE 1. Comparison of details between the simulated image with speckle noise and real sonar image using our proposed FLS noise model. (a) Real FLS image; (b) Simulated FLS image.

Equation (1) can be expressed as Equation (2):

$$\varphi(x, y) = \omega_m(x, y)\psi(x, y) \quad (2)$$

After conducting data statistics and comparing different distributions, a novel Gaussian-distributed multiplicative noise model for FLS images is proposed. According to this model, the multiplicative noise in FLS images follows a Gaussian distribution with a probability density in Equation (3):

$$f(x) = \frac{1}{\sqrt{2\pi}\sigma} \exp\left\{-\frac{(x - \mu)^2}{2\sigma^2}\right\} \quad (3)$$

where μ and σ^2 represent the mean and variance of the distribution. The mean of the Gaussian distribution, which the multiplicative noise adheres to, is set to 1. This choice avoids any shift in the overall pixel value level of the image after introducing noise, thereby preserving the original image information. The variance varies based on different noise intensities.

Therefore, the speckle noise model that interferes with FLS images can be expressed as Equation (4):

$$\varphi(x, y) = \omega_m(x, y)\psi(x, y), \omega_m(x, y) \sim N(1, \sigma^2) \quad (4)$$

To demonstrate the effectiveness of the proposed speckle noise model, we simulated FLS images corrupted with speckle noise based on the model. The results are illustrated in Figure 1.

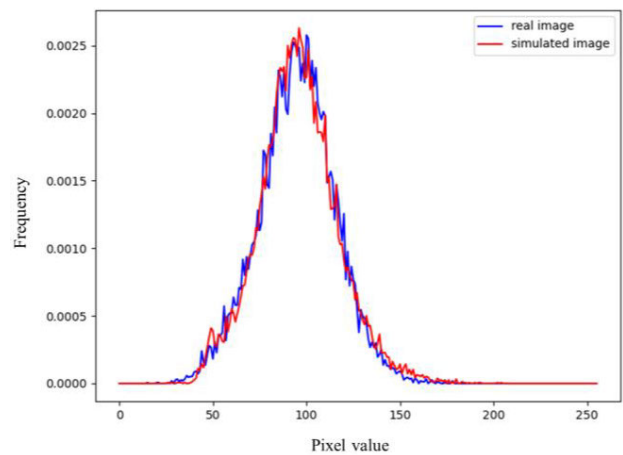


FIGURE 2. Histogram of pixel values in the contrasting regions of the both images.

Since replicating and generating simulated images that perfectly match the content of real sonar images is challenging, we chose uniform regions of the two images that lack edges and textures for comparison. Uniform regions have a concentrated distribution of pixel values and lack structures such as edges that cause abrupt changes in pixel values. Hence, they effectively reflect the distribution characteristics of speckle noise. In Figure 1, the comparison region of the real and simulated sonar images exhibits a highly similar visual effect. Moreover, we calculated and presented the frequency distribution of pixel values in the comparison region by traversing the pixel values of each pixel in both images, as shown in Figure 2.

Figure 2 demonstrates that the simulated and real images share similar distribution characteristics of pixel values. Since the pixel value changes in the contrast region of both images are solely related to multiplicative noise, the identical pixel value distribution confirms that the synthesized image is subject to the same multiplicative noise interference as the real sonar image. It's important to note that the pixel value distributions of the simulated and real images have the same mean value. This was deliberately set during the image synthesis process to align the two pixel value distribution curves at their peak values, making it easier to compare the degree of pixel value dispersion.

III. METHODOLOGY OF LPMsDE

LPMsDE involves addressing two crucial aspects of FLS image quality improvement: denoising and enhancement. Denoising requires finding a balance between reducing noise and preserving important details, while enhancement aims to highlight image features while avoiding amplifying noise [45]. To achieve this, we adopt a multi-scale analysis by decomposing the FLS image into three levels using the Laplacian pyramid framework. Each level contains different scales and characteristics, encompassing noise, edges, textures, and main content. This separation of specific content allows for noise removal while retaining valuable information.

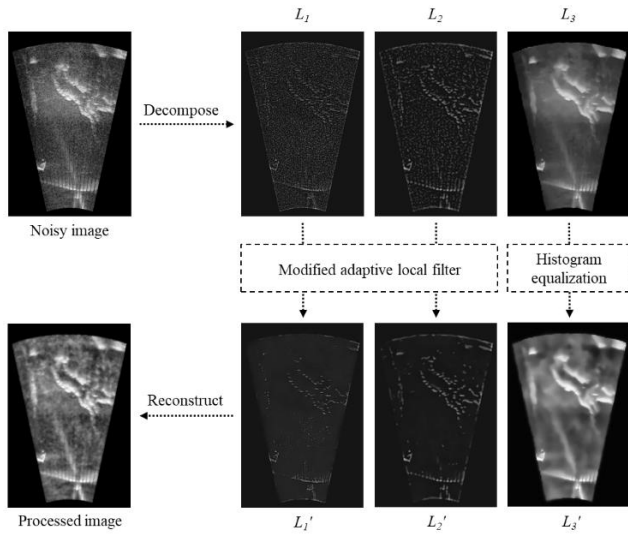


FIGURE 3. Overall flowchart of the proposed LPMsDE method.

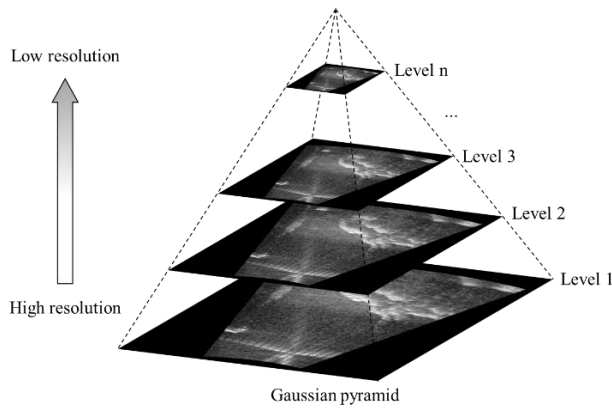


FIGURE 4. Structure of Gaussian pyramid.

To handle the Laplacian images containing noise, we improved the adaptive local filter by combining it with the image characteristics of the Laplacian pyramid. This modified adaptive local filter is applied to denoise the first and second levels of the Laplacian pyramid (L_1 and L_2 in Figure 3). In the highest level of the Laplacian pyramid (L_3), we use contrast-limited histogram equalization (CLHE) to enhance the image contrast and accentuate its features. The algorithmic flow is depicted in Figure 3.

A. LAPLACIAN PYRAMID FRAMEWORK

In the proposed methodology, we utilize the Laplacian pyramid framework for multi-scale representation of FLS images [46]. An image pyramid is a collection of images arranged in a pyramid shape, obtained from the same input image but with varying resolutions. There are two main types of image pyramids: the Laplacian pyramid (LP) and the Gaussian pyramid (GP). The difference between the two pyramids is that all the images of the GP are different resolution representations of the input image, whereas in the images that make up the LP, the higher-level images are computationally obtained

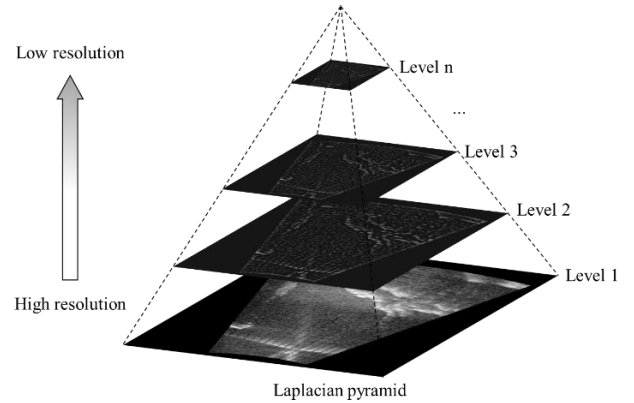


FIGURE 5. Structure of Laplacian pyramid.

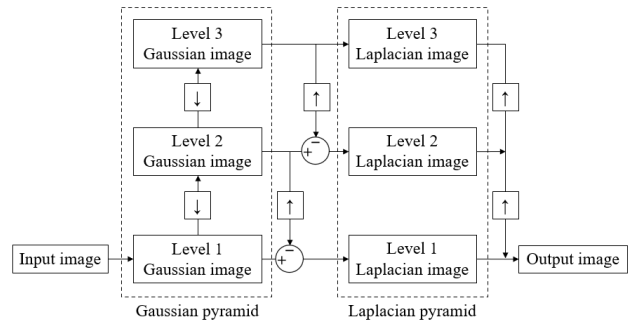


FIGURE 6. Process of image decomposition and reconstruction through image pyramid.

Laplacian images, except for the bottom level, which is the original image. Figure 4 and 5 illustrate the structure of GP and LP, respectively.

Both pyramids decrease in resolution from bottom to top, with the original input image having the highest resolution at the bottom and the lowest resolution representation at the top. Figure 6 illustrates the process of image decomposition and reconstruction using a three-level image pyramid. The up and down arrows represent upsampling and subsampling, respectively.

The GP is generated by successively reducing the scale of the image through Gaussian kernel convolution and subsampling. However, in this paper, to preserve image details and avoid blurring edges and textures, we omit the Gaussian kernel convolution and perform only image subsampling. Let N be the highest level of the GP, then G_n represents the n th level Gaussian image. G_1 is the bottom level of the GP, which is equivalent to the input image. To obtain G_n , we perform subsampling on G_{n-1} , reducing the rows and columns of the image by half, resulting in G_n , which can be represented as Equation (5):

$$G_n(t) = sub(G_{n-1}(t)), 0 < n \leq N \tag{5}$$

where $G(t)$ represents the image generated at time t , and $sub(\cdot)$ denotes subsampling of the image.

During the generation of each level of the GP, approximately three-quarters of the information in the image is lost

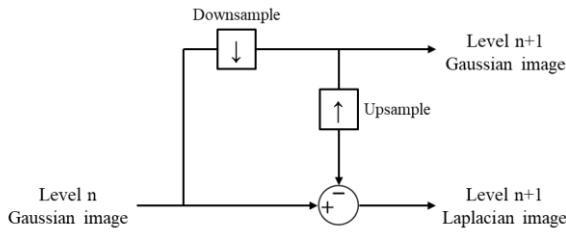


FIGURE 7. Calculation process of Laplacian images.

due to subsampling. To capture and represent this lost information, we define the Laplacian Pyramid (LP). The Laplacian image is obtained by subtracting the upsampled version of the higher level of the GP from the corresponding level of the GP, resulting in a difference image. The flowchart for obtaining the Laplace images through Gaussian images is shown in Figure 7.

The LP consists of L_1, L_2, \dots, L_n and L_n represents the n th level of LP, which can be expressed as Equation (6):

$$L_n(t) = G_n(t) - up(G_{n+1}(t)), 0 \leq n < N \quad (6)$$

where $up(\cdot)$ represents the signal interpolation process applied to the image. The upsampling is performed by interpolation in this case.

The Laplacian pyramid framework decomposes the original FLS image into multiple levels of different scales, comprising a low-frequency subband and multiple high-frequency subbands. The low-frequency component represents the smooth regions of the image, typically containing most of the image energy and corresponding to the background. The pixel intensity distribution of the image is mainly reflected in the low-frequency information. On the other hand, the high-frequency component typically represents high-frequency information, such as edges and noise, and reflects the richness of information at corresponding positions in the image [47]. The higher the absolute value of the high-frequency information, the clearer the details of the image, but it is more susceptible to noise interference. The LP decomposition images have the ability to represent the high-frequency components of the corresponding level of the GP, leading some researchers to refer to this property as the predictive residual effect of the LP [48].

Originally, the LP was designed for image reconstruction from the GP. The reconstructed image is obtained by synthesizing the enhanced subband images in the LP, from the coarsest level to the finest level. The reconstruction process follows the inverse process of the LP decomposition to reconstruct the corresponding GP, and finally, the restored image $G'_1(t)$ is obtained. The reconstruction process can be represented as Equation (7):

$$G'_n(t) = \begin{cases} up(G'_{n+1}(t)) + L_n(t), & 0 \leq n < N \\ G_n(t), & n = N \end{cases} \quad (7)$$

By decomposing the image into multiple scales using LP, different operators can be employed to process the distinct

characteristics of each subband at different frequencies, allowing for targeted image optimization and processing, which can reveal previously unnoticed characteristics of the image.

B. MODIFIED ADAPTIVE LOCAL FILTER

In the Laplacian images the L_1 and L_2 of the LP, which contain high-frequency signals, detail information, and noise exhibit different distribution characteristics, as depicted in Figure 3. Noise is more uniformly distributed throughout the image, while detail information like edges and textures are more concentrated and display local distribution characteristics. To effectively denoise the image, we propose a modified adaptive local filter based on the Laplacian pyramid framework.

The regular adaptive local filter is defined as Equation (8):

$$g'(x, y) = g(x, y) - \frac{\sigma_\eta^2}{\sigma_S^2} [g(x, y) - z_S] \quad (8)$$

where S defines the neighborhood of a rectangular sub-window centered at pixel (x, y) , within which the filter operates; $g(x, y)$ represents the pixel value of the noise image at pixel (x, y) ; σ_η^2 represents the noise variance; The local mean value of the pixel values in S is denoted by z_S , and the local variance is denoted by σ_S^2 .

In the above Equation, $g(x, y)$, z_S , and σ_S^2 can be obtained from the image, and the only value that cannot be directly calculated is the noise variance σ_η^2 . Accurate estimation of the noise variance is crucial for the denoising effectiveness of the adaptive local filter and is a critical step in the entire denoising process [49]. A precise noise variance leads to a highly effective denoising result, while an overly large or small noise variance can result in blurred boundaries or residual noise, respectively. Fortunately, by utilizing the Laplacian pyramid framework, the input image has already been decomposed into Laplacian images. The Laplacian image contains nearly all the noise and some edge information. Therefore, if the noise variance can be estimated based on the Laplacian image, it can significantly improve the accuracy of describing the noise intensity compared to direct estimation.

As obtaining the noise level of a clean real sonar image is not feasible, we can use the speckle noise model established in the previous section. By adding speckle noise to the simulated image, we can obtain both the clean image and the noisy image. The variance of the noise can be represented as the difference between the noisy image and the clean image at each corresponding pixel, with a variance of σ_η^2 , and the variance of the Laplacian image is represented as σ_L^2 . It was observed that under different variances of the Gaussian distribution followed by the speckle noise, i.e., under different noise levels, σ_η^2 and σ_L^2 exhibit a linear relationship, as shown in Figure 8.

Therefore, the variance of noise can be expressed as Equation (9):

$$\sigma_\eta^2 = a\sigma_L^2 + b \quad (9)$$

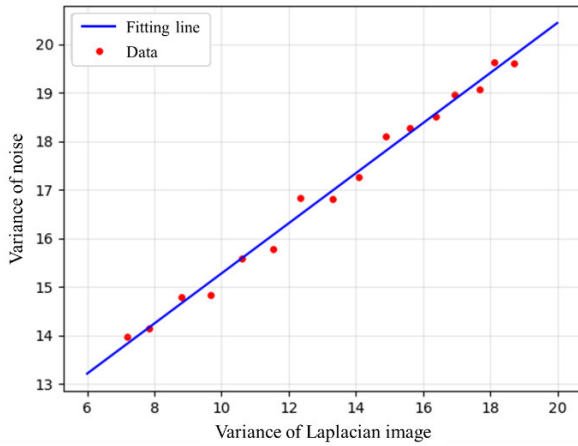


FIGURE 8. Linear relationship between the variance of noise and the variance of Laplacian image.

The modified adaptive local filter can be expressed using Equation (8) and (9) as Equation (10):

$$g'(x, y) = g(x, y) - \frac{a\sigma_L^2 + b}{\sigma_S^2} [g(x, y) - z_S] \quad (10)$$

C. CONTRAST-LIMITED HISTOGRAM EQUALIZATION

In underwater environments, researchers and workers are particularly concerned with the interpretation and recognition of sonar images. In tasks like maritime search and rescue, it is crucial to extract as much potential information of the drowning person from the image as possible, even if they are in non-bright areas of the image. Therefore, feature enhancement is necessary for sonar images to improve image interpretation and recognition by highlighting important information that may have been initially overlooked and making it more prominent. In essence, feature enhancement enhances the quality of the image and increases the amount of information contained in it.

The highest-level image of the LP, which is also the highest-level image of the GP, has undergone two rounds of subsampling. At this point, its resolution is only 1/16 of the original image, and there is almost no high-frequency information (edges and noise), only containing content information at a coarse scale, as shown in Figure 3. To address this characteristic, a histogram equalization (HE) method is used to enhance the contrast of this level of the image, achieving the purpose of feature enhancement.

In sonar images, the background areas, which occupy a large proportion, are usually dominated by dark pixels, while underwater targets have strong grayscale variations. Therefore, when using HE, there may be problems with some areas losing details or becoming noisy due to excessive contrast enhancement [50]. To address this issue, contrast-limited histogram equalization (CLHE) is chosen to enhance low-resolution images. CLHE sets a threshold for the histogram distribution to prevent the influence of excessive contrast in some areas on the image information while ensuring that the

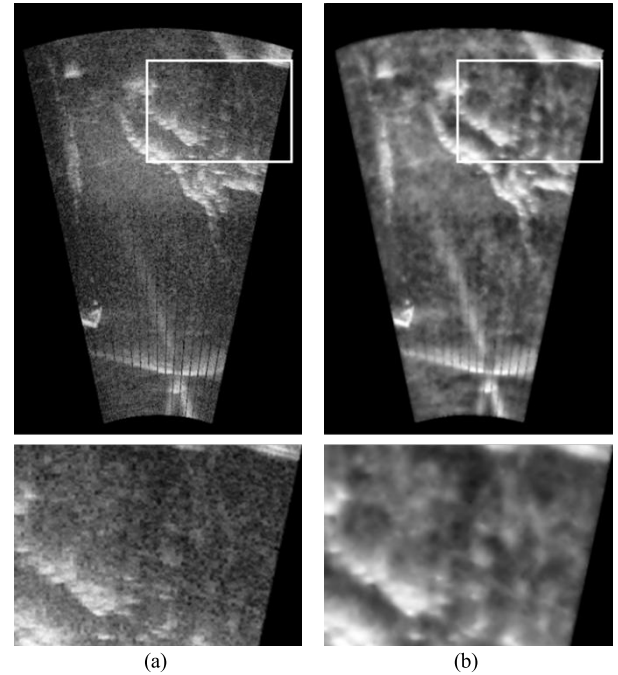


FIGURE 9. Comparison of images before and after CLHE enhancement. (a) Image before CLHE enhancement; (b) Image after CLHE enhancement.

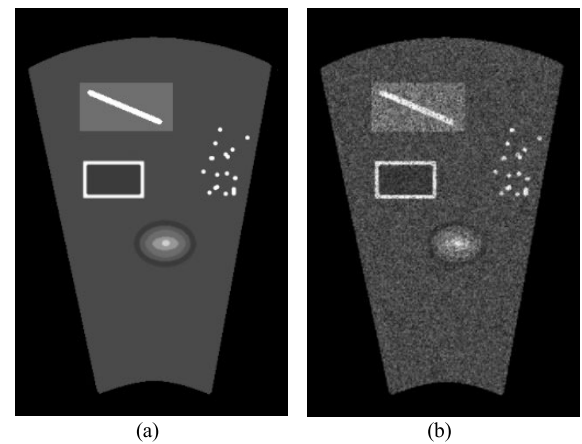


FIGURE 10. Simulated sonar images. (a) Clean image; (b) Noisy image with speckle noise with a variance of 0.4.

integration of the probability density is still 1. The distribution exceeding this threshold is uniformly dispersed on the probability density distribution to limit the amplification of the transfer function (cumulative histogram). This method has a better improvement effect on dark and bright areas. The images before and after enhancement by CLHE are shown in Figure 9.

By combining the Laplacian pyramid framework with CLHE, image features can be enhanced while effectively preventing the phenomenon of noise and features being enhanced together. As shown in Figure 9, the quality of the image after contrast enhancement has been greatly improved compared to the original image. The information in the boxed area was originally not obvious due to being in a darker area of the image, and the specific content was also difficult

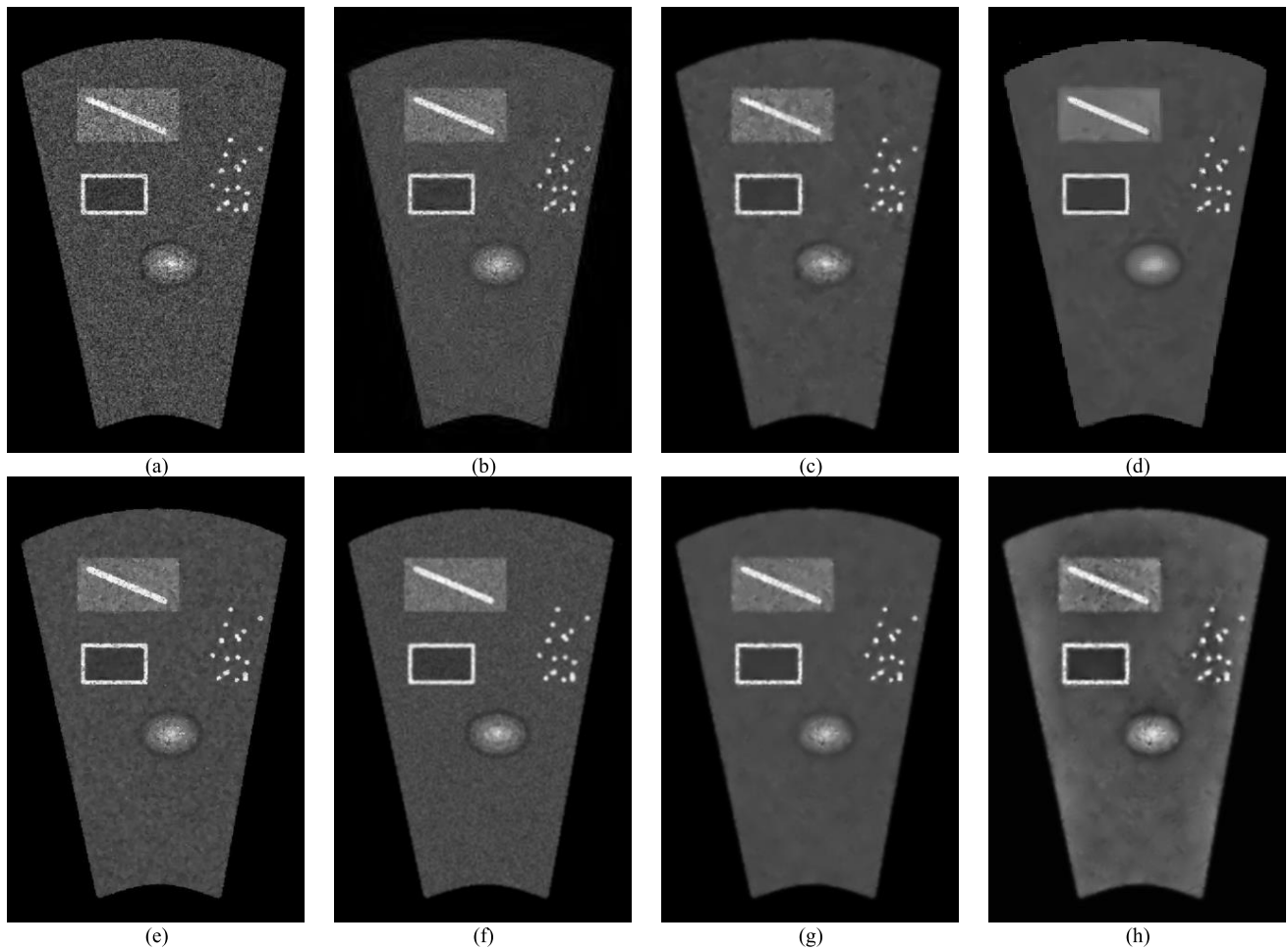


FIGURE 11. Processing results by different methods on simulation sonar image. (a) Noisy image; (b) ST; (c) CSR; (d) IBM3D; (e) ABF; (f) NCC-PDE; (g) LPMsD; (h) LPMsDE.

to discern clearly. After enhancement, the originally low contrast was improved, and the structural information in the dark area became very prominent, while the noise was not enhanced. This approach ensures that important features are enhanced, thereby improving the overall image quality and interpretability for underwater workers and researchers.

IV. EXPERIMENTS AND ANALYSIS

To evaluate the denoising and enhancement capabilities of the proposed method, we conducted two experiments where the LPMsDE was compared with other representative state-of-the-art image processing methods: a simulation study and a real sonar image experiment. The former was used to compare the denoising performance of different methods using SSIM and PSNR as metrics. The latter compared the feature enhancement performance by contrasting CNR, ENL, NIQE, and BRISQUE.

All experimental outcomes presented in this paper were obtained on a platform equipped with an Intel Core i5 12400 CPU, NVIDIA RTX 4060 GPU, Win10 64-bit operating system, Python 3.8 and Matlab 2016b.

A. SIMULATED SONAR IMAGE EXPERIMENT

To generate the simulated sonar image, we created a synthetic image based on some characteristics of FLS images, including common shapes, and matched the size of real sonar images used in subsequent experiments. Subsequently, we subjected the clean image to 9 levels of speckle noise, with variance ranging from 0.1 to 0.9, following the speckle noise model proposed in Section II. Figure 10 (a) illustrates the clean image, while Figure 10 (b) depicts the noisy image with speckle noise added, with a variance of 0.4.

The proposed method was compared with other denoising algorithms based on non-convex constrained PDE (NCC-PDE) [51], adaptive bilateral filter (ABF) [52], shearlet transform (ST) [25], convolutional sparse representation (CSR) [14], and the improved BM3D (IBM3D) [13]. Figure 11 displays the processing results for the simulated image with speckle noise at a variance of 0.4. The results are represented by (a)-(h), corresponding to the unprocessed noisy image, other denoising methods for comparison, the proposed LPMsD (denoising only) and the LPMsDE (denoising and enhancement), respectively.

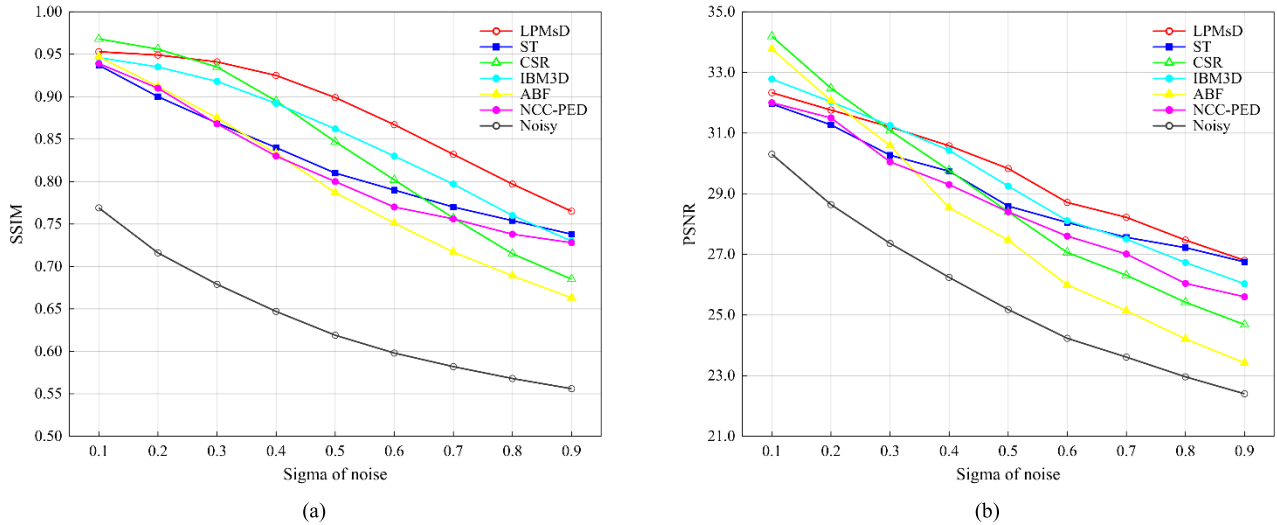


FIGURE 12. SSIM and PSNR values of denoised simulated images with different noise intensities. (a) SSIM; (b) PSNR.

To compare the denoising performance of different methods, we employed two objective evaluation metrics: the Structural Similarity Index (SSIM) and Peak Signal-to-Noise Ratio (PSNR), both widely used for assessing the effectiveness of image denoising. SSIM, being a full-reference image quality evaluation index, aligns better with human visual perception habits [53]. This method evaluates image quality by comparing the structural features of the original image and the noisy image, with a higher SSIM value indicating better preservation of image structure by the denoising method. PSNR, initially used to represent the relationship between the maximum signal value and background noise, later found application in comparing similarity between two images. It is expressed on a logarithmic scale, with a higher PSNR value suggesting stronger similarity between two images. A common benchmark for PSNR is 30dB, with images having PSNR values below 30dB considered significantly habits [53]. Given that the LPMsDE significantly alters the pixel values of the image during the enhancement process, SSIM and PSNR are not applicable to it, and only the LPMsD was compared. The images with nine different noise intensities were processed by different methods, and their SSIM and PSNR values were calculated with respect to the clean image, as shown in Figure 12.

According to the comparison results of denoised images in Figure 11 and the different algorithms in terms of SSIM and PSNR in Figure 12, some conclusions can be drawn. There is some residual noise in the image processed by the ST method (Figure 11 (b)), which is dense and has a very small particle size. This situation is particularly evident at low noise levels (noise sigma \leq 0.7), but as the noise intensity increases, the residual noise becomes less. The values of SSIM and PSNR confirm this situation, that is, the index values at low noise levels are lower than other methods, but they surpass other methods at high noise levels. We believe that it is because high-intensity noise is more easily separated after

undergoing shearlet transform, making the ST method more suitable for processing high-intensity noise. The CSR method exhibits the opposite performance to the ST method: it has a significant advantage in dealing with low-intensity noise, but its objective index values rapidly decrease as the noise intensity increases. As shown in Figure 11 (c), the image processed by the CSR method has many randomly distributed local pixel value mutations. Perhaps, as mentioned in [14], the CSR method is more suitable for processing Gaussian noise and impulse noise in sonar images. IBM3D exhibits a very strong denoising performance, as the speckle noise is almost imperceptible to the naked eye in Figure 11 (d). Especially in the elliptical area with gradient colors, it achieves amazing denoising effects. However, more artifacts, such as blocky or streaky color patches, appear in uniform pixel value areas (gray background). Nevertheless, thanks to its powerful denoising performance, IBM3D maintains good results in objective index evaluations, second only to the proposed method in this paper. The ABF method (Figure 11 (e)) performs best in edge preservation, but the noise is not completely eliminated while preserving clear edges. In addition to residual speckle noise, black and white pixels similar to impulse noise also appear in the image. We speculate that this is due to the failure to handle individual pixels with large changes in value during bilateral filtering. The residual noise not only affects the visual effect of the image but also ranks the ABF method last in objective index comparison. The NCC-PDE method (Figure 11 (f)) shares the same problem with the ST and ABF methods, as it fails to completely eliminate speckle, resulting in noticeable residual noise. However, unlike the latter two methods, the residual noise after NCC-PDE processing is more evenly distributed and the pixel value mutations are not as severe. In addition, the NCC-PDE method performs well in edge preservation, resulting in a visually softer image. The NCC-PDE method also ranks in the middle in terms of SSIM and PSNR.

From a visual perspective, the LPMsD method (Figure 11 (g)) achieves a compromise between noise suppression and edge preservation. Although it inevitably blurs some edges, such as the white line and rectangle in the image, which are not as clear as those in the ABF and NCC-PDE methods, its denoising effect is significantly better than the latter two methods. It is worth noting that in uniform regions, the LPMsD method exhibits the best noise suppression performance, with neither too much residual noise nor any artifacts. We speculate that this is the main reason for its excellent performance in objective index evaluation. As shown in Figure 12, except for the first two noise levels, the LPMsD method consistently outperforms the other methods in terms of SSIM and PSNR. We believe that LPMsD is more capable of eliminating medium-to-high intensity noise, which is common in actual FLS images, making it a powerful tool for FLS image denoising. In addition, it can be observed in Figure 11 (h) that the LPMsDE method significantly improves the contrast of the image compared to the LPMsD, especially in areas with alternating brightness, such as the rectangles and spots in the image. As a result, the LPMsDE method significantly enhances image features, making it easier to interpret FLS images.

B. REAL SONAR IMAGE EXPERIMENT

Real FLS sonar image experiments were used to compare the performance of different feature enhancement methods. The real sonar images were provided by Deepak Singh from “Marine Debris Dataset for Forward-Looking Sonar” [54]. The dataset was collected using an ARIS Explorer 3000 FLS, containing a total of 1868 FLS images. We carefully selected 50 images with an image size of 480×320 .

We compared our proposed LPMsDE method with the currently most advanced CLAHE and alpha-rooting methods. As a classic histogram equalization method, the CLAHE algorithm and its modifications limit the histogram of each sub-block, resulting in a more natural image contrast. Alpha-rooting is one of the more popular frequency domain enhancement methods. It uses transformation in the frequency domain through modification magnitudes and altering the frequency content of the image [55]. The results of applying the PLT-CLAHE [56], multi-scale alpha-rooting [57], generalized alpha-rooting [58], and LPMsDE methods to enhance real FLS images are shown in Figure 13.

Objective evaluation methods for image quality are typically divided into three categories: full-reference (FR), reduced-reference (RR), and no-reference (NR) methods. When evaluating image quality, FR and RR image quality metrics require high-quality reference images, either in full or in part. Unfortunately, real FLS images do not have natural reference images for comparison. To fully understand the performance of the compared image enhancement methods, we selected four NR metrics: Contrast-to-Noise Ratio (CNR), Equivalent Number of Looks (ENL), Natural Image Quality Evaluator (NIQE), and Blind/Referenceless Image Spatial Quality Evaluator (BRISQUE).

TABLE 1. Non-reference measures for real sonar image.

	CNR	ENL	NIQE	BRISQUE
Original	2.26	12.85	4.25	33.27
Multi-scale alpha-rooting	4.96	13.89	3.92	31.06
PLT-CLAHE	6.41	13.52	4.16	31.40
Generalized alpha-rooting	7.04	14.40	3.77	29.57
LPMsDE	6.87	15.00	3.38	28.32

We applied enhancement methods to the 50 images and evaluated the results using no-reference metrics, as shown in Table 1. The results in Table 1 represent the average values of the scores in 50 FLS images after enhancement.

Figure 13 and Table 1 demonstrate the performance comparison of different enhancement methods. The images processed by the two alpha-rooting methods (Figure 13 (b) and (d)) have similar characteristics, namely, they both enhance the contrast of the image to some extent. However, both methods significantly increase speckle noise while highlighting the target, which affects the visual effect of the image. It can be seen that the difference between the two methods is the degree of enhancement of the image. The multi-scale alpha-rooting method has a slightly lower contrast enhancement compared to the generalized alpha-rooting method and the former is less affected by noise. In terms of objective evaluation, except for CNR, the scores of the other indicators for both methods are relatively similar, ranking third and fourth, respectively. It is worth mentioning that the generalized alpha-rooting method obtained the highest CNR value, proving that its image has the highest contrast. The PLT-CLAHE method (Figure 13 (c)), an improvement on the classic contrast enhancement algorithm CLAHE, did not achieve the desired effect in highlighting image features. Excessive brightness compensation instead led to a decrease in contrast in some areas of the image. Nevertheless, the PLT-CLAHE method still showed improvement in no-reference evaluation metric scores compared to the original image, albeit ranking lower. We speculate that this is due to the brightness compensation reducing the impact of existing speckle noise on the image to some extent, resulting in a higher score.

The proposed LPMsDE method (Figure 13 (e)) benefits from the Laplacian pyramid framework, which decomposes the image into multiple levels and applies multi-scale processing to each level. This approach simultaneously enhances contrast of the main content, suppresses noise, and preserves detail information. As a result, it meets the requirements for feature enhancement in FLS image interpretation while preventing noise from masking valid information in the image. In addition to CNR, the LPMsDE method outperforms other methods in the remaining three objective indicators,

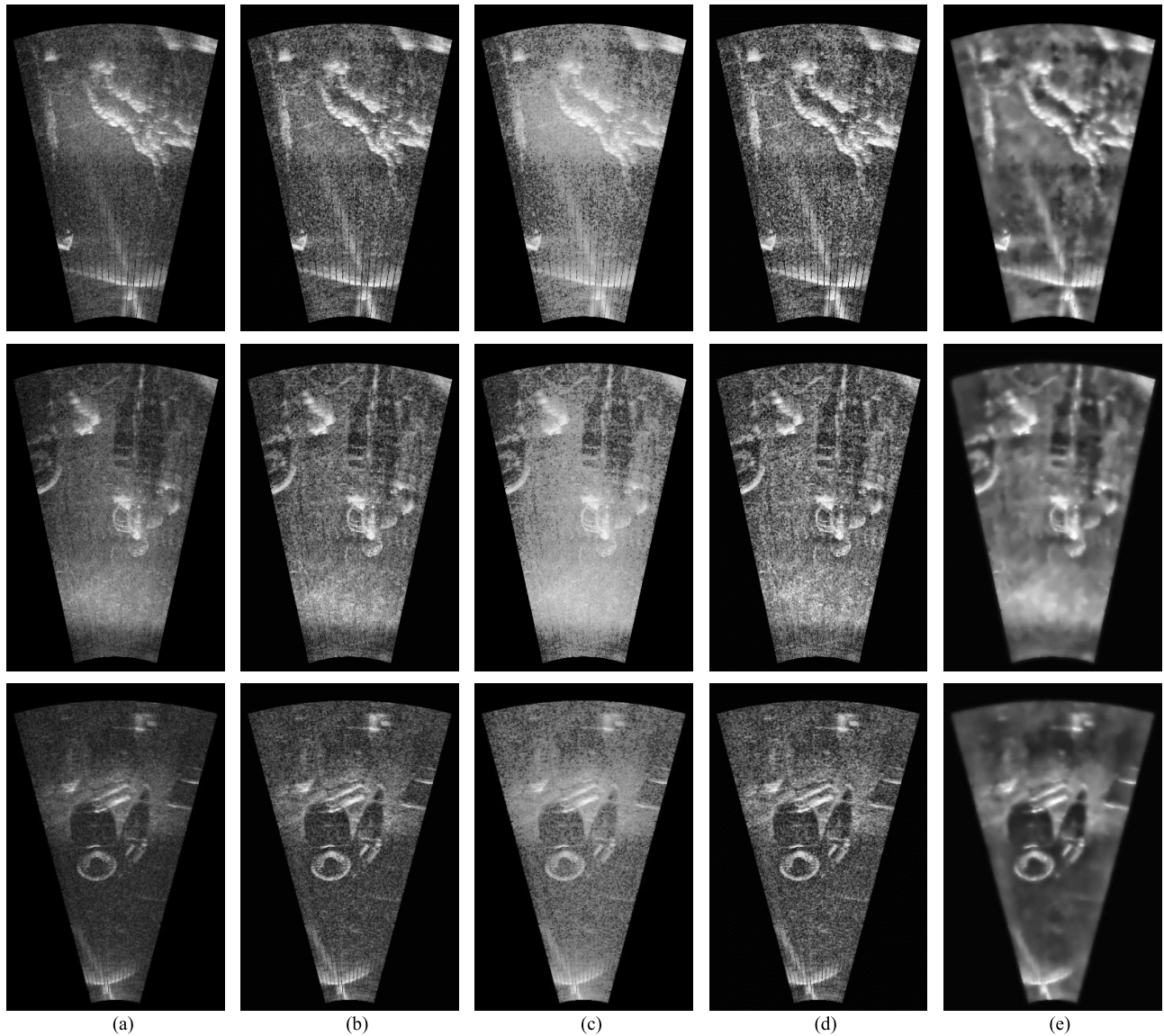


FIGURE 13. Processing results by different methods on real sonar images. (a) Original images; (b) Multi-scale alpha-rooting; (c) PLT-CLAHE; (d) Generalized alpha-rooting; (e) LPMsDE.

demonstrating its superior enhancement effect. The method of simultaneously denoising and enhancing by first layering the image, then performing multi-scale analysis and processing, and finally reconstructing the image is more effective than combining separate denoising and enhancement methods, whether denoising is performed before or after enhancement. The former inevitably loses some valid information during the denoising process, which remains missing after enhancement, while the latter amplifies noise and significantly increases the difficulty of denoising.

V. CONCLUSION

This paper introduces a novel multi-scale denoising and enhancement method, LPMsDE, specifically designed for forward-looking sonar images. The proposed approach involves several key steps. Firstly, the image is decomposed into two high-frequency components and one low-frequency

component using the Laplacian pyramid framework, effectively separating noise, edges, textures, and main content. Secondly, a modified adaptive local filter, in conjunction with the Laplacian pyramid framework, is employed to calculate the noise variance of the image based on the generated Laplacian image. To establish the mapping relationship between the Laplacian image and the noise variance, the FLS image multiplicative noise model, adhering to the Gaussian distribution, is utilized. Lastly, the modified adaptive local filter and the contrast-limited histogram equalization algorithm are applied to denoise and enhance the high-frequency and low-frequency components, respectively. comprehensive experiments demonstrate the superiority of the LPMsDE method in both denoising and enhancement.

Looking ahead, future research will concentrate on the following aspects: finding faster and more effective image processing modules for the Laplacian pyramid framework,

and exploring the optimal combination of denoising and enhancement algorithms. By combining the proposed method with deep neural networks and leveraging the concept of multi-scale analysis, we aim to develop a more advanced denoising network with superior performance.

ACKNOWLEDGMENT

The authors would like to express their gratitude to Chen Huang, Han Xue, and Xin Su from the National Engineering Research Center for Water Transport Safety for scoring their experimental results.

REFERENCES

- [1] H. Zhang, M. Tian, G. Shao, J. Cheng, and J. Liu, "Target detection of forward-looking sonar image based on improved YOLOv5," *IEEE Access*, vol. 10, pp. 18023–18034, 2022, doi: [10.1109/ACCESS.2022.3150339](https://doi.org/10.1109/ACCESS.2022.3150339).
- [2] N. Palomeras, T. Furfaro, D. P. Williams, M. Carreras, and S. Dugelay, "Automatic target recognition for mine countermeasure missions using forward-looking sonar data," *IEEE J. Ocean. Eng.*, vol. 47, no. 1, pp. 141–161, Jan. 2022, doi: [10.1109/JOE.2021.3103269](https://doi.org/10.1109/JOE.2021.3103269).
- [3] Z. Wang, S. Zhang, W. Huang, J. Guo, and L. Zeng, "Sonar image target detection based on adaptive global feature enhancement network," *IEEE Sensors J.*, vol. 22, no. 2, pp. 1509–1530, Jan. 2022, doi: [10.1109/JSEN.2021.3131645](https://doi.org/10.1109/JSEN.2021.3131645).
- [4] T. Zhou, J. Si, L. Wang, C. Xu, and X. Yu, "Automatic detection of underwater small targets using forward-looking sonar images," *IEEE Trans. Geosci. Remote Sens.*, vol. 60, 2022, Art. no. 4207912, doi: [10.1109/TGRS.2022.3181417](https://doi.org/10.1109/TGRS.2022.3181417).
- [5] J.-S. Lee, "Speckle analysis and smoothing of synthetic aperture radar images," *Comput. Graph. Image Process.*, vol. 17, no. 1, pp. 24–32, 1981, doi: [10.1016/S0146-664X\(81\)80005-6](https://doi.org/10.1016/S0146-664X(81)80005-6).
- [6] V. S. Frost, J. A. Stiles, K. S. Shanmugan, and J. C. Holtzman, "A model for radar images and its application to adaptive digital filtering of multiplicative noise," *IEEE Trans. Pattern Anal. Mach. Intell.*, vol. PAMI-4, no. 2, pp. 157–166, Mar. 1982, doi: [10.1109/TPAMI.1982.4767223](https://doi.org/10.1109/TPAMI.1982.4767223).
- [7] D. Kuan, A. Sawchuk, T. Strand, and P. Chavel, "Adaptive restoration of images with speckle," *IEEE Trans. Acoust., Speech, Signal Process.*, vol. ASSP-35, no. 3, pp. 373–383, Mar. 1987, doi: [10.1109/TASSP.1987.1165131](https://doi.org/10.1109/TASSP.1987.1165131).
- [8] M. Zhang and B. K. Gunturk, "Multiresolution bilateral filtering for image denoising," *IEEE Trans. Image Process.*, vol. 17, no. 12, pp. 2324–2333, Dec. 2008, doi: [10.1109/TIP.2008.2006658](https://doi.org/10.1109/TIP.2008.2006658).
- [9] M. Elad, "On the origin of the bilateral filter and ways to improve it," *IEEE Trans. Image Process.*, vol. 11, no. 10, pp. 1141–1151, Oct. 2002, doi: [10.1109/tip.2002.801126](https://doi.org/10.1109/tip.2002.801126).
- [10] A. Buades, B. Coll, and J.-M. Morel, "A non-local algorithm for image denoising," in *Proc. IEEE Comput. Soc. Conf. Comput. Vis. Pattern Recognit.*, Jun. 2005, pp. 60–65, doi: [10.1109/CVPR.2005.38](https://doi.org/10.1109/CVPR.2005.38).
- [11] K. Dabov, A. Foi, V. Katkovnik, and K. Egiazarian, "Image denoising by sparse 3-D transform-domain collaborative filtering," *IEEE Trans. Image Process.*, vol. 16, no. 8, pp. 2080–2095, Aug. 2007, doi: [10.1109/TIP.2007.901238](https://doi.org/10.1109/TIP.2007.901238).
- [12] A. Abu and R. Diamant, "Robust image denoising for sonar imagery," in *Proc. Oceans*, May 2018, pp. 1–5, doi: [10.1109/OCEANS-KOBE.2018.8559398](https://doi.org/10.1109/OCEANS-KOBE.2018.8559398).
- [13] X. Han, Q. Sun, Y. Li, and F. Ye, "A novel sonar image denoising algorithm based on block matching," in *Proc. Int. Conf. Microw. Millim. Wave Technol. (ICMMT)*, Aug. 2022, pp. 1–3, doi: [10.1109/ICMMT55580.2022.10023281](https://doi.org/10.1109/ICMMT55580.2022.10023281).
- [14] A. Vishwakarma, "Denoising and inpainting of sonar images using convolutional sparse representation," *IEEE Trans. Instrum. Meas.*, vol. 72, pp. 1–9, 2023, doi: [10.1109/TIM.2023.3246527](https://doi.org/10.1109/TIM.2023.3246527).
- [15] A. Saurabh, A. Kumar, and U. Anitha, "Performance analysis of various wavelet thresholding techniques for despeckling of sonar images," in *Proc. 3rd Int. Conf. Signal Process., Commun. Netw. (ICSCN)*, Mar. 2015, pp. 1–7, doi: [10.1109/ICSCN.2015.7219869](https://doi.org/10.1109/ICSCN.2015.7219869).
- [16] C. Stolojescu-Crisan and C. Botoca, "SONAR images restoration in the wavelets domain," in *Proc. 12th IEEE Int. Symp. Electron. Telecommun. (ISETC)*, Oct. 2016, pp. 265–268, doi: [10.1109/ISETC.2016.7781108](https://doi.org/10.1109/ISETC.2016.7781108).
- [17] P. Xia, Q. Ren, D.-X. Shi, B.-J. Lei, Y.-B. Zou, and G.-Z. Xu, "Low SNR sonar image restoration based on mixed probability statistical model in wavelet domain," in *Proc. IEEE Int. Conf. Parallel Distrib. Process. Appl., Big Data Cloud Comput., Sustain. Comput. Commun., Social Comput. Netw.*, Dec. 2019, pp. 1457–1465, doi: [10.1109/ISPA-BDCloud-SustainCom-SocialCom48970.2019.00210](https://doi.org/10.1109/ISPA-BDCloud-SustainCom-SocialCom48970.2019.00210).
- [18] H. Liu, F. Yang, S. Zheng, Q. Li, D. Li, and H. Zhu, "A method of side-lobe effect suppression for multibeam water column images based on an adaptive soft threshold," *Appl. Acoust.*, vol. 148, pp. 467–475, May 2019, doi: [10.1016/j.apacoust.2019.01.006](https://doi.org/10.1016/j.apacoust.2019.01.006).
- [19] R. James and M. H. Supriya, "Sonar image denoising using adaptive processing of local patches," in *Proc. Int. Symp. Ocean Electron. (SYMPOL)*, Nov. 2015, pp. 1–7, doi: [10.1109/sympol.2015.7581165](https://doi.org/10.1109/sympol.2015.7581165).
- [20] F. Yin, C. Li, H. Wang, and F. Yang, "Automatic tracking of weak acoustic targets within jamming environment by using image processing methods," *Appl. Sci.*, vol. 12, no. 13, p. 6698, Jul. 2022, doi: [10.3390/app12136698](https://doi.org/10.3390/app12136698).
- [21] W. Chen, Z. Liu, H. Zhang, M. Chen, and Y. Zhang, "A submarine pipeline segmentation method for noisy forward-looking sonar images using global information and coarse segmentation," *Appl. Ocean Res.*, vol. 112, Jul. 2021, Art. no. 102691, doi: [10.1016/j.apor.2021.102691](https://doi.org/10.1016/j.apor.2021.102691).
- [22] T. Xinyu, Z. Xuewu, X. Xiaolong, S. Jinbao, and X. Yan, "Methods for underwater sonar image processing in objection detection," in *Proc. Int. Conf. Comput. Syst., Electron. Control (ICCSEC)*, Dec. 2017, pp. 941–944, doi: [10.1109/ICCSEC.2017.8446701](https://doi.org/10.1109/ICCSEC.2017.8446701).
- [23] D. Wu, X. Du, and K. Wang, "An effective approach for underwater sonar image denoising based on sparse representation," in *Proc. IEEE 3rd Int. Conf. Image. Vis. Comput. (ICIVC)*, Jun. 2018, pp. 389–393, doi: [10.1109/ICIVC.2018.8492877](https://doi.org/10.1109/ICIVC.2018.8492877).
- [24] K. Landmark, A. H. Schistad Solberg, F. Albrechtsen, A. Austeng, and R. E. Hansen, "A radon-transform-based image noise filter—With applications to multibeam bathymetry," *IEEE Trans. Geosci. Remote Sens.*, vol. 53, no. 11, pp. 6252–6273, Nov. 2015, doi: [10.1109/TGRS.2015.2436380](https://doi.org/10.1109/TGRS.2015.2436380).
- [25] H. Zhang, J. Cheng, M. Tian, J. Liu, G. Shao, and S. Shao, "A reverberation noise suppression method of sonar image based on shearlet transform," *IEEE Sensors J.*, vol. 23, no. 3, pp. 2672–2683, Feb. 2023, doi: [10.1109/JSEN.2022.3229406](https://doi.org/10.1109/JSEN.2022.3229406).
- [26] S. Li, J. Zhao, H. Zhang, Z. Bi, and S. Qu, "A non-local low-rank algorithm for sub-bottom profile sonar image denoising," *Remote Sens.*, vol. 12, no. 14, p. 2336, Jul. 2020, doi: [10.3390/rs12142336](https://doi.org/10.3390/rs12142336).
- [27] W. Tian, Z. Chen, J. Shen, F. Huang, and L. Xu, "Underwater sonar image denoising through nonconvex total variation regularization and generalized Kullback–Leibler fidelity," *J. Ambient Intell. Humanized Comput.*, vol. 13, no. 11, pp. 5237–5251, Nov. 2022, doi: [10.1007/s12652-021-03420-5](https://doi.org/10.1007/s12652-021-03420-5).
- [28] H.-Y. Yan and Y.-M. Huang, "Cauchy noise removal by a generalized nonlocal low-rank method," *J. Electron. Imag.*, vol. 31, no. 3, pp. 1–12, May 2022, doi: [10.1117/1.jei.31.3.033022](https://doi.org/10.1117/1.jei.31.3.033022).
- [29] Y. Zhang, Y. Tian, Y. Kong, B. Zhong, and Y. Fu, "Residual dense network for image restoration," *IEEE Trans. Pattern Anal. Mach. Intell.*, vol. 43, no. 7, pp. 2480–2495, Jul. 2021, doi: [10.1109/TPAMI.2020.2968521](https://doi.org/10.1109/TPAMI.2020.2968521).
- [30] L. Donati, T. Fontanini, F. Tagliaferri, and A. Prati, "An energy saving road sweeper using deep vision for garbage detection," *Appl. Sci.*, vol. 10, no. 22, p. 8146, Nov. 2020, doi: [10.3390/app10228146](https://doi.org/10.3390/app10228146).
- [31] Y. Amit, P. Felzenszwalb, and R. Girshick, "Object detection," in *Computer Vision*. Cham, Switzerland: Springer, 2020, pp. 1–9, doi: [10.1007/978-3-030-03243-2_660-1](https://doi.org/10.1007/978-3-030-03243-2_660-1).
- [32] J. Kim, S. Song, and S.-C. Yu, "Denoising auto-encoder based image enhancement for high resolution sonar image," in *Proc. IEEE Underwater Technol. (UT)*, Feb. 2017, pp. 1–5, doi: [10.1109/UT.2017.7890316](https://doi.org/10.1109/UT.2017.7890316).
- [33] M. Sung, H. Cho, T. Kim, H. Joe, and S.-C. Yu, "Crosstalk removal in forward scan sonar image using deep learning for object detection," *IEEE Sensors J.*, vol. 19, no. 21, pp. 9929–9944, Nov. 2019, doi: [10.1109/JSEN.2019.2925830](https://doi.org/10.1109/JSEN.2019.2925830).
- [34] H. Xu, L. Zhang, M. J. Er, and Q. Yang, "Underwater sonar image segmentation based on deep learning of receptive field block and search attention mechanism," in *Proc. 4th Int. Conf. Intell. Auton. Syst. (ICoIAS)*, May 2021, pp. 44–48, doi: [10.1109/ICoIAS53694.2021.00016](https://doi.org/10.1109/ICoIAS53694.2021.00016).
- [35] B. Lee, B. Ku, W. Kim, S. Kim, and H. Ko, "Feature sparse coding with CoordConv for side scan sonar image enhancement," *IEEE Geosci. Remote Sens. Lett.*, vol. 19, pp. 1–5, 2022, doi: [10.1109/LGRS.2020.3026703](https://doi.org/10.1109/LGRS.2020.3026703).

- [36] K. Cheng, L. Yan, Y. Ding, H. Zhou, M. Li, and H. A. Ghafoor, "Sonar image garbage detection via global despeckling and dynamic attention graph optimization," *Neurocomputing*, vol. 529, pp. 152–165, Apr. 2023, doi: [10.1016/j.neucom.2023.01.081](https://doi.org/10.1016/j.neucom.2023.01.081).
- [37] X. Zhou, C. Yu, X. Yuan, and C. Luo, "Deep denoising method for side scan sonar images without high-quality reference data," in *Proc. 2nd Int. Conf. Comput., Control Robot. (ICCCR)*, Mar. 2022, pp. 241–245.
- [38] R. James and M. H. Supriya, "Blind estimation of single look side scan sonar image from the observation model," *Proc. Comput. Sci.*, vol. 93, pp. 336–343, Jan. 2016, doi: [10.1016/j.procs.2016.07.218](https://doi.org/10.1016/j.procs.2016.07.218).
- [39] Y. Lu, M. Yang, and R. W. Liu, "DSPNet: Deep learning-enabled blind reduction of speckle noise," in *Proc. 25th Int. Conf. Pattern Recognit. (ICPR)*, Jan. 2021, pp. 3475–3482, doi: [10.1109/ICPR48806.2021.9413017](https://doi.org/10.1109/ICPR48806.2021.9413017).
- [40] Y. Huang, W. Li, and F. Yuan, "Speckle noise reduction in sonar image based on adaptive redundant dictionary," *J. Mar. Sci. Eng.*, vol. 8, no. 10, p. 761, Sep. 2020, doi: [10.3390/jmse8100761](https://doi.org/10.3390/jmse8100761).
- [41] F. Yuan, F. Xiao, K. Zhang, Y. Huang, and E. Cheng, "Noise reduction for sonar images by statistical analysis and fields of experts," *J. Vis. Commun. Image Represent.*, vol. 74, Jan. 2021, Art. no. 102995, doi: [10.1016/j.jvcir.2020.102995](https://doi.org/10.1016/j.jvcir.2020.102995).
- [42] C. A. Duarte-Salazar, A. E. Castro-Ospina, M. A. Becerra, and E. Delgado-Trejos, "Speckle noise reduction in ultrasound images for improving the metrological evaluation of biomedical applications: An overview," *IEEE Access*, vol. 8, pp. 15983–15999, 2020, doi: [10.1109/ACCESS.2020.2967178](https://doi.org/10.1109/ACCESS.2020.2967178).
- [43] M. V. Perera, N. G. Nair, W. G. C. Bandara, and V. M. Patel, "SAR despeckling using a denoising diffusion probabilistic model," *IEEE Geosci. Remote Sens. Lett.*, vol. 20, pp. 1–5, 2023, doi: [10.1109/LGRS.2023.3270799](https://doi.org/10.1109/LGRS.2023.3270799).
- [44] Q. Wu, H. Zhang, Z. Lai, Y. Xu, S. Yao, and J. Tao, "An enhanced data-driven array shape estimation method using passive underwater acoustic data," *Remote Sens.*, vol. 13, no. 9, p. 1773, May 2021, doi: [10.3390/rs13091773](https://doi.org/10.3390/rs13091773).
- [45] X. Liu, M. Pedersen, and R. Wang, "Survey of natural image enhancement techniques: Classification, evaluation, challenges, and perspectives," *Digit. Signal Process.*, vol. 127, Jul. 2022, Art. no. 103547, doi: [10.1016/j.dsp.2022.103547](https://doi.org/10.1016/j.dsp.2022.103547).
- [46] J. Kang, J. Y. Lee, and Y. Yoo, "A new feature-enhanced speckle reduction method based on multiscale analysis for ultrasound B-mode imaging," *IEEE Trans. Biomed. Eng.*, vol. 63, no. 6, pp. 1178–1191, Jun. 2016, doi: [10.1109/TBME.2015.2486042](https://doi.org/10.1109/TBME.2015.2486042).
- [47] C. Tian, M. Zheng, W. Zuo, B. Zhang, Y. Zhang, and D. Zhang, "Multi-stage image denoising with the wavelet transform," *Pattern Recognit.*, vol. 134, Feb. 2023, Art. no. 109050, doi: [10.1016/j.patcog.2022.109050](https://doi.org/10.1016/j.patcog.2022.109050).
- [48] T. Zhang and X. Zhang, "Squeeze-and-Excitation Laplacian pyramid network with dual-polarization feature fusion for ship classification in SAR images," *IEEE Geosci. Remote Sens. Lett.*, vol. 19, pp. 1–5, 2022, doi: [10.1109/LGRS.2021.3119875](https://doi.org/10.1109/LGRS.2021.3119875).
- [49] H. Zhang, Y. Zhu, and H. Zheng, "NAMF: A nonlocal adaptive mean filter for removal of salt-and-pepper noise," *Math. Problems Eng.*, vol. 2021, pp. 1–10, Mar. 2021, doi: [10.1155/2021/4127679](https://doi.org/10.1155/2021/4127679).
- [50] A. K. Bhandari and S. Maurya, "Cuckoo search algorithm-based brightness preserving histogram scheme for low-contrast image enhancement," *Soft Comput.*, vol. 24, no. 3, pp. 1619–1645, Feb. 2020, doi: [10.1007/s00500-019-03992-7](https://doi.org/10.1007/s00500-019-03992-7).
- [51] A. Hadri, L. Afraites, A. Laghrib, and M. Nachaoui, "A novel image denoising approach based on a non-convex constrained PDE: Application to ultrasound images," *Signal, Image Video Process.*, vol. 15, no. 5, pp. 1057–1064, Jul. 2021, doi: [10.1007/s11760-020-01831-z](https://doi.org/10.1007/s11760-020-01831-z).
- [52] H. Li and X.-L. Duan, "SAR ship image speckle noise suppression algorithm based on adaptive bilateral filter," *Wireless Commun. Mobile Comput.*, vol. 2022, pp. 1–10, Aug. 2022, doi: [10.1155/2022/9392648](https://doi.org/10.1155/2022/9392648).
- [53] D. R. I. M. Setiadi, "PSNR vs SSIM: Imperceptibility quality assessment for image steganography," *Multimedia Tools Appl.*, vol. 80, no. 6, pp. 8423–8444, Mar. 2021, doi: [10.1007/s11042-020-10035-z](https://doi.org/10.1007/s11042-020-10035-z).
- [54] D. Singh and M. Valdenegro-Toro, "The marine debris dataset for forward-looking sonar semantic segmentation," in *Proc. IEEE/CVF Int. Conf. Comput. Vis. Workshops (ICCVW)*, Oct. 2021, pp. 3734–3742, doi: [10.1109/ICCVW54120.2021.00417](https://doi.org/10.1109/ICCVW54120.2021.00417).
- [55] V. Voronin, A. Zelensky, and S. Agaian, "3-D block-rooting scheme with application to medical image enhancement," *IEEE Access*, vol. 9, pp. 3880–3893, 2021, doi: [10.1109/ACCESS.2020.3047461](https://doi.org/10.1109/ACCESS.2020.3047461).
- [56] Q. Fu, M. Celenk, and A. Wu, "An improved algorithm based on CLAHE for ultrasonic well logging image enhancement," *Cluster Comput.*, vol. 22, no. S5, pp. 12609–12618, Sep. 2019, doi: [10.1007/s10586-017-1692-8](https://doi.org/10.1007/s10586-017-1692-8).
- [57] V. V. Voronin, E. Semenishchev, A. Zelensky, and S. Agaian, "Image enhancement through multi-scale alpha-rooting processing for remote sensing application," *Proc. SPIE*, vol. 11510, pp. 715–721, Sep. 2020, doi: [10.1117/12.2571601](https://doi.org/10.1117/12.2571601).
- [58] A. M. Grigoryan and S. S. Agaian, "Alpha-rooting and correlation method of image enhancement," *Proc. SPIE*, vol. 12100, pp. 147–156, May 2022, doi: [10.1117/12.2617434](https://doi.org/10.1117/12.2617434).



water image denoising and enhancement, and underwater 3D reconstruction.

ZHISEN WANG was born in Henan, China, in 1998. He received the bachelor's degree in marine engineering from the Wuhan University of Technology, in 2021, where he is currently pursuing the M.S. degree in traffic and transportation engineering.

He is a member of the State Key Laboratory of Maritime Technology and Safety, Wuhan University of Technology. His research interests include intelligent underwater perception, underwater image denoising and enhancement, and underwater 3D reconstruction.



international Society for Underwater Technology (China) Technical Conference.

ZHUOYI LI received the B.Sc. degree in road bridge and river-crossing engineering and the M.S. degree in intelligent transportation and safety from the School of Transportation, Wuhan University of Technology, Wuhan, China, in 2018. He is currently pursuing the Ph.D. degree with The Hong Kong Polytechnic University. His research interests include computer vision, sonar denoising, and sonar target detection. He received the Outstanding Student Presentation of the 11th International Society for Underwater Technology (China) Technical Conference.



XUANXUAN TENG received the M.S. degree from the Kitami Institute of Technology, in 2009, and the Ph.D. degree in systems science and informatics from Hokkaido University, in 2012. She is currently a Lecturer with the College of Electrical and Electronic, Wuhan Polytechnic University. Her research interests include intelligent underwater vehicles, nonlinear controller design, and networked control systems.



DESHAN CHEN was born in Anhui, China, in 1986. He received the M.S. degree in information and computing science from Jilin University, in 2009, and the Ph.D. degree in systems science and informatics from Hokkaido University, in 2014.

He is currently an Associate Professor with the Intelligent Transportation Systems Center, Wuhan University of Technology. His research interests include intelligent maritime supervision, intelligent underwater perception, computer vision, and pattern recognition.

Prof. Chen received the Best Paper Award from *Measurement Science and Technology*, in 2015, and the China Navigation Society Award, in 2018.

• • •